Chapter 3

MATERIALS AND METHODOLOGY

This chapter describes the raw materials and experimental procedures employed in the development of various Ti alloys. It includes detailed characterizations and experiments carried out, including phase composition, microstructural analysis, physical, mechanical, tribological, electrochemical corrosion, tribocorrosion, and biological behaviour to investigate their suitability for biomedical implant applications.

3.1 Materials

In the present study, three types of alloys have been developed for biomedical implant applications: binary Ti-alloys (Ti-Nb and Ti-Zr alloys), ternary Ti-alloys (Ti-Zr-Nb alloys), and high entropy alloys incorporating Ti, Nb, Zr, Mo, Cu, and Sn. The details of each material are provided in Table 3.1. X-ray diffraction and SEM analysis was conducted to verify the purity and morphology of the powders before their use, which are shown in Fig. 3.1 and Fig. 3.2 respectively. In addition, to compare the properties of the developed alloys with commercially available implant materials, cpTi and Ti-6Al-4V plates were procured and their details are also included in Table 3.1.

Table 3.1: Details of elemental raw material used for development of the alloys

Materials	Size	Morphology	Purity	Physical state	Supplier
Ti	≤ 44 µm	Irregular	99.99%	Powder	Alfa Aesar, UK
Nb	≤ 44 µm	Irregular	99.99%	Powder	Alfa Aesar, UK
Zr	≤ 44 µm	Irregular	99.99%	Powder	Alfa Aesar, UK
Mo	≤ 5 µm	Irregular	99.9%	Powder	Sigma Aldrich, USA
Cu	≤ 74 µm	Spherical	99.9%	Powder	Alfa Aesar, UK
Sn	≤ 44 µm	Nearly spherical	99.8%	Powder	Alfa Aesar, UK
cpTi	15/20 mm	Solid	Grade 4	Solid	Nextgen Steel & Alloys, India
Ti-6Al-4V	15/20 mm	Solid	Grade 5	Solid	Nextgen Steel & Alloys, India

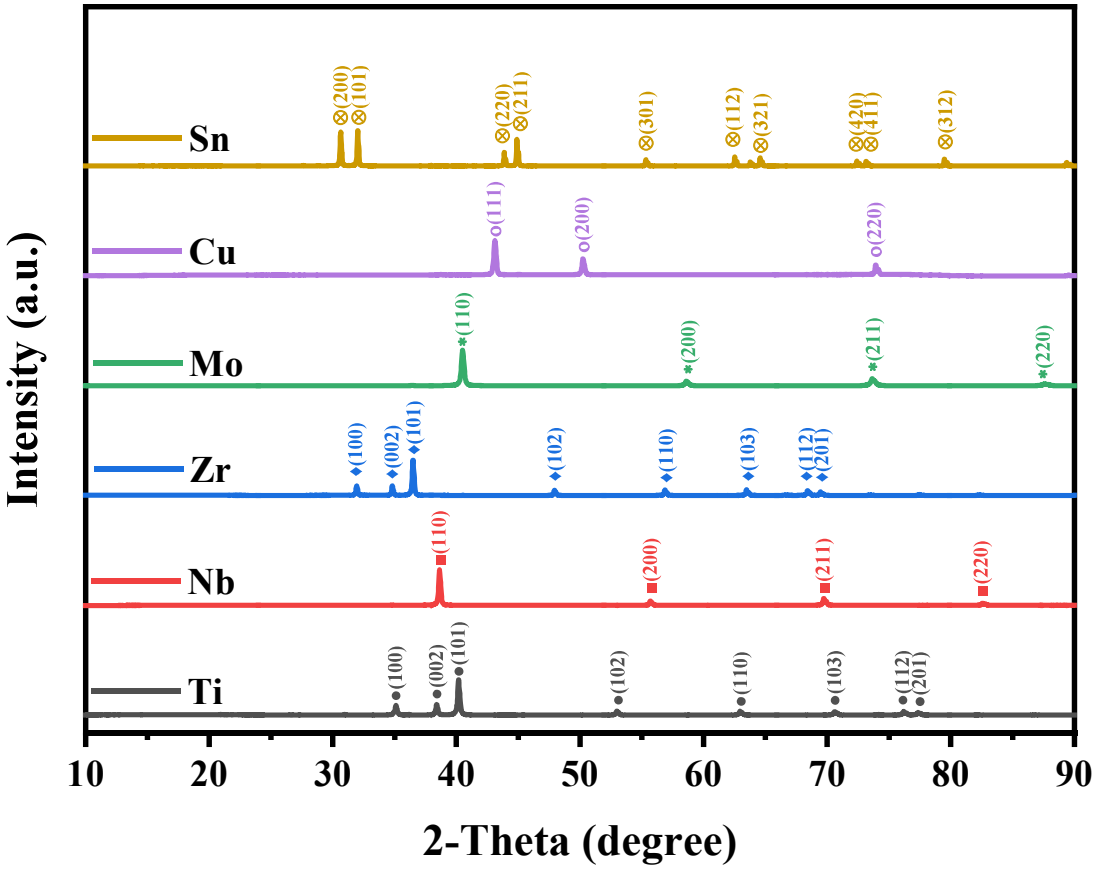

Fig. 3.1: XRD patterns of raw elemental powders

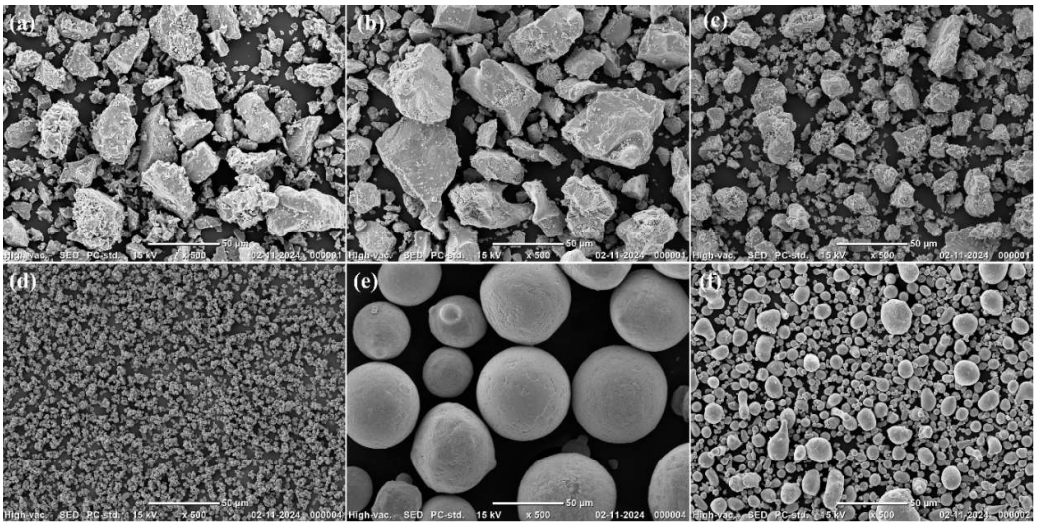

Fig. 3.2: SEM images of raw elemental powders (a) Ti (b) Nb (c) Zr (d) Mo (e) Cu (f) Sn

3.2 Powder metallurgy processing of binary, ternary, and high entropy alloys

3.2.1 Development of binary and ternary alloys

Titanium is highly oxidative element, which reacts with oxygen and makes their oxide very easily. Therefore, the binary and ternary Ti alloys were fabricated through a unique approach of vacuum sealing in a quartz tube. The schematic flow diagram of the processing of different Ti alloys are shown in Fig. 3.3. In this technique, firstly the raw powders were taken in require quantity as per the specific composition and placed in a tungsten carbide jar with tungsten carbide balls of 5 mm and 10 mm diameters for milling in a high energy planetary ball milling machine. The milling was carried out in an inert argon atmosphere with toluene as a process control agent. The toluene which is used as a process control agent prevents overheating and undesirable reactions among the powder particles. Toluene plays a crucial role in preventing cold welding of the powder particles by forming a thin protective layer on their surfaces. This layer acts as a lubricant, which reduces agglomeration and minimize friction and heat generation during the milling process. Additionally, it helps to control contamination from the

milling media and the environment by acting as a barrier, thereby reducing the likelihood of oxidation and other unwanted chemical reactions. By facilitating better mixing, toluene also improves the overall efficiency of the milling process. The milling process was carried out at 200 rpm sun speed and 400 rpm jar speed for 7.5 hours, where it is set to 15 min pause after every 30 min run. The milling process helps to achieve a uniform distribution of elemental powders and refine their particle size, thereby enhancing contact between particles and enabling efficient solid-state diffusion during sintering. After this, the milled powders were subjected to compaction at 650 MPa compaction pressure to obtain the green compact except Ti-10Zr-xNb alloys, which was compacted at 600 MPa for increased porosity. These green compacts were inserted in different quartz tubes with one side closed and one side with neck connected with an ultrahigh vacuum unit. Once, the vacuum reaches at 10^{-6} torr, the neck was closed by melting and rotation process. The quartz tube, sealed under vacuum with the sample inside, was placed in a muffle furnace for sintering. The temperature was raised at a rate of 5 °C/min until it reached 1000 °C, where it was maintained for 90 minutes. Afterward, the furnace was allowed to cool naturally to room temperature. Under high-vacuum conditions, sintering facilitates interdiffusion among the constituent elements through grain boundary and lattice diffusion, resulting in the formation of solid solutions or intermetallic phases. The vacuum environment minimizes oxidation, thereby preserving chemical purity and enhancing densification. Finally, the samples were retrieved by breaking the quartz tube and were used for further characterization and testing. The sintering temperature of 1000 °C was selected because the phase transformation temperature of titanium occurs at approximately 882 °C. Sintering below this temperature may lead to incomplete phase transformation and immature microstructure formation. A sintering temperature of 1000 °C for 90 minutes, with a

heating rate of 5 °C/min, was sufficient to promote interdiffusion and densification while minimizing excessive grain growth. This choice aligns with similar studies on titanium-based systems, which suggest that these parameters effectively balance densification and microstructural control. Moreover, the consistent heating rate of 5 °C/min was chosen to ensure uniform thermal distribution and reduce thermal stresses within the compact, in line with previous studies recommended [168]. Repeating the same procedure several samples were prepared with 15 mm and 20 mm diameters for microstructural, physical, mechanical, tribological, and tribocorrosion testing. The one set of powder metallurgy processed samples are shown in Fig. 3.4.

3.2.2 Development of high entropy alloys

The development of high entropy alloys involves selection of elemental powders and design through empirical relations. Therefore, the design and synthesis are separately discussed in sections 3.2.2.1 and 3.2.2.2.

3.2.2.1 Design of high entropy alloys

Designing a high entropy alloy (HEA) involves determining the constituent elements and optimizing their composition. To achieve a stable solid solution, several key parameters must be optimized, including the entropy of mixing, enthalpy of mixing, atomic size factor, and valence electron concentration. These values must fall within defined ranges to promote the formation of a solid solution. Empirical formulas to predict phase stability and lattice structure in HEAs are given below [103].

Entropy of mixing

The entropy of mixing for the alloys system is given by Eq. (3.1).

$$\Delta S_{mix} = -R \sum_{i=1}^{n} (c_i \ln c_i) \quad (3.1)$$

Where, ΔS_{mix}, R, and c_i denote the entropy of mixing, the universal gas constant, and the atomic percentage of the ith element in the alloy, respectively. The universal gas

constant *R* has a value of 8.314.

Enthalpy of mixing

The enthalpy of mixing for the alloys system is calculated by the Eq. (3.2):

$$\Delta H_{mix} = \sum_{i=1,j\neq i}^{n} 4\,\Delta H_{mix}^{AB}(c_i c_j) \quad (3.2)$$

Where, ΔH_{mix}, H_{mix}^{AB}, and c_j represent the enthalpy of mixing, enthalpy of mixing of the binary alloy system, and atomic percentage of the jth element respectively.

Atomic size factor

The atomic size factor of the alloy system, represented by δ, is calculated by Eq. (3.3):

$$\delta = \sqrt{\sum_{i=1}^{n} c_i \left(1 - \frac{r_i}{\bar{r}}\right)^2} \quad (3.3)$$

The average atomic radius of the alloy system, denoted by $\bar{r}$, is calculated by expression $\bar{r} = \sum_{i=1}^{n} c_i r_i$. Where, r_i represents the atomic radius of the ith element.

Valance electron concentration

The valance electron concentration, represented by VEC, is commonly used to predict the crystal structure of an alloy and is calculated by Eq. (3.4).

$$VEC = \sum_{i=1}^{n} c_i (VEC)_i \quad (3.4)$$

Where, $(VEC)_i$ represents the VEC of ith element.

Based on empirical observations, a VEC of 8 or higher typically leads to the formation of a face-centered cubic (FCC) structure, while a VEC of less than 6.87 tends to result in a body-centered cubic (BCC) structure.

The aim of the present study is to design the high entropy alloys with BCC structure to get the reduced elastic modulus. The design criteria are as follow:

(a) Design of $TiNb_{1.5}Mo_{1.1}Zr_{1.15}Cu_{0.25}$ HEA

The atomic percentages, atomic radius, and VEC of various elements for

$TiNb_{1.5}Mo_{1.1}Zr_{1.15}Cu_{0.25}$ HEA are listed in Table 3.2 and the enthalpy of mixing values of the binary alloy system are provided in Table 3.3.

Table 3.2: Atomic percentage, atomic radius, and VEC of various elements in $TiNb_{1.5}Mo_{1.1}Zr_{1.15}Cu_{0.25}$ HEA

Element	Quantity	Atomic percentage	r_i (Å)	VEC of element
Ti	1	$\frac{1}{1+1.5+1+1.5+0.25}=0.2$	1.4615	4
Nb	1.5	$\frac{1.5}{1+1.5+1+1.5+0.25}=0.3$	1.4290	5
Mo	1.1	$\frac{1.1}{1+1.5+1+1.5+0.25}=0.22$	1.3626	6
Zr	1.15	$\frac{1.15}{1+1.5+1+1.5+0.25}=0.23$	1.6025	4
Cu	0.25	$\frac{0.25}{1+1.5+1+1.5+0.25}=0.05$	1.279	11

Table 3.3: Enthalpy of mixing of binary alloys (ΔH_{ij}^{mix}, kJ/mol) for $TiNb_{1.5}Mo_{1.1}Zr_{1.15}Cu_{0.25}$ HEA, following Miedema's approach

Element	Ti	Nb	Mo	Zr	Cu
Ti	-	1.975	-0.222	-3.507	-8.855
Nb	1.975	-	3.945	-5.583	2.535
Mo	-0.222	3.945	-	-5.988	-22.413
Zr	-3.507	-5.583	-5.988	-	18.489
Cu	-8.855	2.535	-22.413	18.489	-

(b) Design of $TiNbZr_{0.8}Mo_{0.92}Sn_{0.28}$ HEA

The atomic percentages, atomic radius, and VEC of various elements for $TiNb_{1.5}Mo_{1.1}Zr_{1.15}Cu_{0.25}$ HEA are listed in Table 3.4 and the enthalpy of mixing values

of the binary alloy system are provided in Table 3.5.

Table 3.4: Atomic percentage, atomic radius, and VEC of various elements in $TiNbZr_{0.8}Mo_{0.92}Sn_{0.28}$ HEA

Element	Quantity	Atomic percentage	r_i (Å)	VEC of element
Ti	1	$\frac{1}{1+1+0.8+0.92+0.28} = 0.25$	1.4615	4
Nb	1.5	$\frac{1}{1+1+0.8+0.92+0.28} = 0.25$	1.4290	5
Zr	0.8	$\frac{1}{1+1+0.8+0.92+0.28} = 0.2$	1.6025	4
Mo	0.92	$\frac{1}{1+1+0.8+0.92+0.28} = 0.23$	1.3626	6
Sn	0.25	$\frac{1}{1+1+0.8+0.92+0.28} = 0.07$	1.62	4

Table 3.5: Enthalpy of mixing of binary alloys (ΔH_{ij}^{mix}, kJ/mol) for $TiNbZr_{0.8}Mo_{0.92}Sn_{0.28}$ HEA, following Miedema's approach

Element	Ti	Nb	Zr	Mo	Sn
Ti	-	1.975	-3.507	-0.222	-34.341
Nb	1.975	-	-5.583	3.945	-14.420
Zr	-3.507	-5.583	-	-5.988	-57.527
Mo	-0.222	3.945	-5.988	-	7.338
Sn	-34.341	-14.420	-57.527	7.338	-

The values of entropy of mixing, enthalpy of mixing, atomic size factor, and valence electron concentration for $TiNb_{1.5}Mo_{1.1}Zr_{1.15}Cu_{0.25}$ HEA and $TiNbZr_{0.8}Mo_{0.92}Sn_{0.28}$ HEA are calculated using Eq. (3.1) to (3.4), based on the parameters provided in Table 3.2 to 3.5. The corresponding results are summarized in Table 3.6.

Table 3.6: Design parameters of $TiNb_{1.5}Mo_{1.1}Zr_{1.15}Cu_{0.25}$ and $TiNbZr_{0.8}Mo_{0.92}Sn_{0.28}$ HEAs

Sample	Entropy of mixing (J/K.mol.)	Enthalpy of mixing (KJ/mol.)	Valance electron concentration	Atomic size factor
$TiNb_{1.5}Mo_{1.1}Zr_{1.15}Cu_{0.25}$	12.504	-4.40145	5.09	6.4%
$TiNbZr_{0.8}Mo_{0.92}Sn_{0.28}$	12.797	-16.2327	4.71	5.8054%

3.2.2.2 Sample preparation

The preparation of high entropy alloys follows the similar procedure to that of binary and ternary alloys such as milling, compaction, and sintering. However, the milling was performed for a longer duration to achieve the mechanical alloying of five different elements. The total effective milling was performed up to 45 hours for $TiNb_{1.5}Mo_{1.1}Zr_{1.15}Cu_{0.25}$ and 50 hours for $TiNbZr_{0.8}Mo_{0.92}Sn_{0.28}$ high entropy alloys. A small portion of powder is taken out form the jar at 15 minutes, 5, 15, 25, 35, 45 and 50 hours for the phase analysis. Every time when jar opened argon gas filled again before continuing milling process. The long duration milling process involve, repeated cold welding, fracturing, and re-welding of the multi-elemental powders induce severe plastic deformation and generate a high density of crystalline defects. These conditions significantly enhance atomic mobility and promote the formation of a metastable supersaturated solid solution even at room temperature. After 50 hours of milling process jars were allowed to cool at room temperature, then the mixed powder was taken out and dried in oven at 70 °C for 24 hours to completely remove the moisture content from the powder. After that, these powders were compacted at 650 MPa and sintered in a high vacuum of 10^{-6} torr sealed in the quartz tube. The sintering of the high entropy alloys was tried at the same parameter as of binary and ternary alloys. However, the same parameters of sintering process were not sufficient for the processing of these

high entropy alloys. The high entropy alloys developed in previous studies has either followed melting technique or through mechanical alloying and spark plasma sintering. However, no literature based on mechanical alloying and conventional sintering has been found. In the present study, various sintering temperature were varied to achieve the desired sample properties. During multiple attempts, the sintering of the high entropy alloy was carried out in two steps; step 1: Heating with 5 °C per minute and holding at 900 °C for 13 hours and then, step 2: Heated up to 1000 °C with a heating rate of 5 °C per minute and holding time for 4.5 hours [169]. During sintering, further diffusion and atomic rearrangement occur, driving the transformation of these metastable phases into stable or near-equilibrium multi-phase or single-phase HEA structures. After sintering, the sample was allowed to cool inside the furnace. Once room temperature was reached, the quartz tube was broken and the sintered samples were removed from the furnace. Once the sample was obtained, it further used for different characterization and testing. These parameters were useful in obtaining the dense and desirable samples. So, this is an original and own optimized parameter for processing of these composition of HEA.

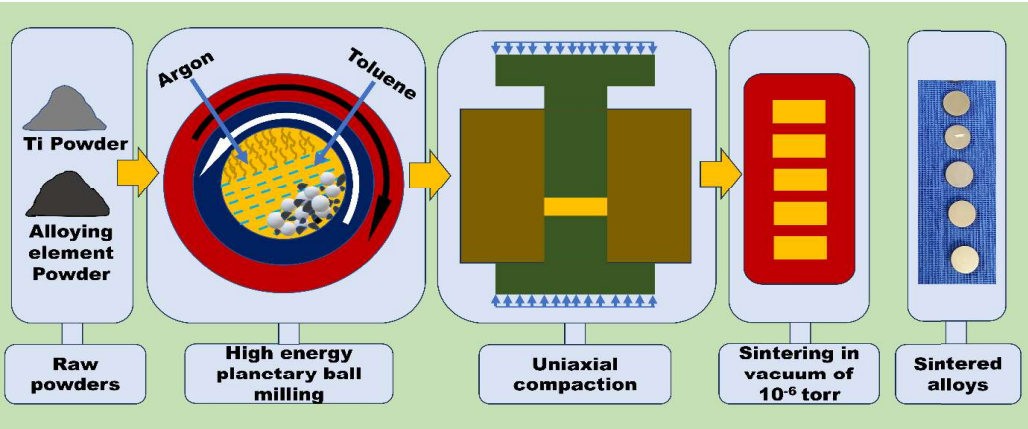

Fig. 3.3: Schematic diagram of Ti alloys processing through powder metallurgy technique

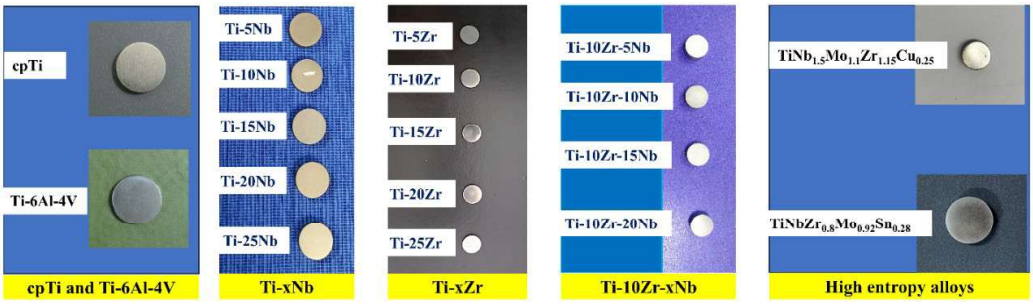

Fig. 3.4: Image of actual powder metallurgy processed samples

3.3 Phase composition and microstructure

3.3.1 X-ray diffraction analysis for phase composition

The phase composition of raw powders, ball milled powders, and sintered solid samples was determined using X-ray diffraction (XRD) analysis. This analysis helps to identify the phases and crystal structure present in the powders and sintered alloys. It was carried out with an X-ray diffractometer (Miniflex 600 Desktop, Rigaku corporation, Tokyo, Japan) shown in Fig. 3.5 with a scanning speed of 5°/min in the 2-theta ranging between 10°-90° using Ni-filtered Cu-Kα emission (λ= 1.5406Å) operating at 40KV/15 mA. Bragg's law was used to calculate the inter-planer spacing (d) for all intensity peaks and corresponding 2-Theta are given in Eq. (3.5).

$$n\lambda = 2d\sin\theta \tag{3.5}$$

Where, θ represents the incident angle, λ represents wavelength of X-ray, and n representing an order of the diffraction.

The obtained patterns from XRD were analyzed through X-pert High Score software.

Fig. 3.5: Image of bench top X-ray diffraction instrument

3.3.2 Microstructural analysis by scanning electron microscopy

The microstructure of each type of samples was obtained through scanning electron microscopy imaging (EVO - SEM MA 15/18, Carl Zeiss Microscopy Ltd, and HRSEM-Nova Nano SEM 450, FEI, USA). To obtain the microstructure, the samples were grinded through SiC abrasive papers from 320, 400, 600, 800, 1000, 1500, 2000, and 2500 grit and polished by diamond paste and aerosol spray on a polishing cloth until a mirror finished surface was achieved. Once, the mirror finished surface obtained, it was cleaned in an ultrasonic bath for 30 minutes to remove the surface contamination. After that, the samples were etched through Kroll's reagent (92% distilled water, 6% Nitric acid, and 2% Hydrofluoric acid) for 5 seconds at room temperature. After etching, the samples were rinsed with distilled water and dried using warm air. The SEM image of the etched samples was taken at different magnification to get the microstructure of the developed alloys.

3.4 Density and porosity

The sintered density was determined according with ASTM B962, specifically designed for measuring the sintered density of PM products based on the Archimedes

principle, setup shown in Fig. 3.6 (Contech Instrument Ltd., India). Theoretical density and porosity percentage were subsequently calculated by the formulas given in Eq. (3.6) and Eq. (3.7), respectively.

$$\rho_{Th} = \frac{1}{\left(\frac{m_{Ti}}{\rho_{Ti}} + \frac{m_{Nb}}{\rho_{Nb}}\right)} \tag{3.6}$$

$$Porosity\ (\%) = \left(1 - \frac{\rho}{\rho_{Th}}\right) \times 100 \tag{3.7}$$

In this context, m_{Ti} and m_{Nb} denote the mass fraction, while ρ_{Ti} and ρ_{Nb} represent the densities of titanium and niobium powder, respectively. The symbol ρ_{Th} signifies the theoretical density, and ρ denotes the sintered density of the sample.

Fig. 3.6: Density measuring device based on Archimedes principle

3.5 Mechanical properties

3.5.1 Hardness

The microhardness of each sample was assessed using the Vickers hardness tester (Semi-automatic, Micro Mach Technologies, India) shown in Fig. 3.7 at 0.2 kg of load and dwell time of 10 seconds. Impressions were generated by a 136° pyramidal

diamond indenter, resulting in square pyramid impressions. The diagonal lengths of these impressions were determined through optical images, enabling the subsequent calculation of Vickers hardness using the formula specified in Eq. (3.8).

$$HV = 1.8544 \frac{\mathrm{F}}{d^2} \tag{3.8}$$

Here, the average diagonal length (d) is measured in millimeters, and F is the applied force in kgf.

Fig. 3.7: Vickers hardness tester

3.5.2 Elastic modulus

The elastic modulus of all the alloys was determined using an instrumented indentation test conducted with a micro-indentation instrument (MHT^3, Anton Paar GmbH, Germany). The experimental setup for the test is illustrated in Fig. 3.8. The instrument employs the Oliver and Pharr method, a widely recognized technique for evaluating the elastic modulus from the load-displacement data obtained during indentation [170,171]. This method involves analyzing the unloading curve to derive the elastic modulus (E), which is then used to calculate the contact area and, subsequently, the elastic modulus.

Fig. 3.8: Microindentation test setup

3.6 Electrochemical corrosion test

The corrosion behaviour of the developed alloys was assessed using well known electrochemical techniques i.e., open circuit potential (OCP), electrochemical impedance spectroscopy (EIS), potentiodynamic polarization (PDP) test. Where, OCP defines as the stable potential or the voltage difference exists between the electrodes of an electrochemical cell or system when no current is flowing. It represents the natural electrochemical potential of a sample in a specific environment without external polarization, with no net transfer of electrons or ions between the electrodes. Moreover, the Electrochemical Impedance Spectroscopy (EIS) test is conducted to evaluate the impedance of an electrochemical system over a range of frequencies, offering insights into corrosion mechanisms and kinetics. In contrast, the Potentiodynamic Polarization (PDP) test provides a quantitative evaluation of the corrosion rate, typically expressed in millimeters per year (mm/year). The test setup of electrochemical corrosion instrument is shown in Fig. 3.9. The experimental configurations employed a standard three-electrode system electrochemical workstation (CS2350, Wuhan Corrtest Instruments Corp., Ltd., China), utilizing a saturated Ag/AgCl electrode as the reference, platinum wire as the counter electrode, and a 1 cm^2 specimen as the working

electrode. The SBF solution was used as electrolyte, which was prepared in-house by dissolving the reagents given in Table 3.7 in a sequential order [172]. The OCP measurements were recorded over 60 minutes, followed by EIS tests covering a frequency range of 10^{-2} Hz to 10^{5} Hz and an amplitude modulation of alternating current between -10 mV and +10 mV. Subsequently, PDP analysis was performed within the potential range of -1.5 V to +2.4 V and at a scan rate of 1 mV/s. The EIS data were analyzed using Nyquist and Bode plots for understanding the corrosion response of the alloys. Additionally, corrosion kinetics were studied by extracting parameters utilizing the Tafel extrapolation approach, improving our understanding of corrosion processes, such as corrosion potential (E_{corr}) and corrosion current density (I_{corr}).

Table 3.7: Constituents and their quantity of simulated body fluid solution [172]

Reagents	**Amount in 1 Litre (in gram)**
NaCl	8.035
$NaHCO_3$	0.355
KCl	0.225
$K_2HPO_4 \cdot 3H_2O$	0.231
$MgCl_2 \cdot 6H_2O$	0.311
1.0 M HCl	39 ml
$CaCl_2$	0.292
Na_2SO_4	0.072
$(NH_2C(CH_2OH)_3)$	6.118
1.0 M HCl	Drops to adjust pH 7.4

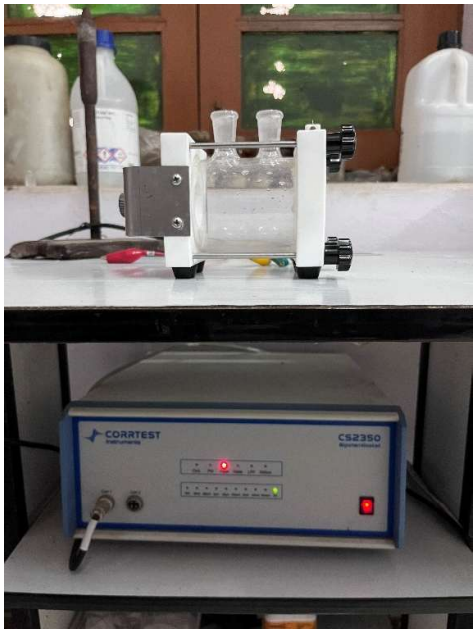

Fig. 3.9: Corr test electrochemical potentiostat corrosion measuring device

3.7 Tribological testing

The tribological testing of these alloys were performed to evaluate the wear resistance and frictional behavior for dental and orthopedic implant materials under simulated physiological conditions. The tribological investigation was carried out using a Bio-tribometer (TR-01, DUCOM Instruments Pvt. Ltd., India) under reciprocating linear motion at 37 ± 1 °C in SBF conditions. The experimental test setup of Bio-tribometer and corresponding wear track formation is shown in Fig. 3.10. The experiments were performed using a 15 mm disc sample and a zirconia ball as counter material with a diameter of 10 mm, subjected to 10 to 40 N of normal load and 5 mm of sliding distance over 3600 cycles. Throughout the tests, the machine control units monitored the frictional force and coefficient of friction (COF) on a per-second basis. The average COF for each sample is reported based on their recorded values. Additionally, the wear volume was determined through an analytical method based on Eq. (3.9) as reported by Z. Doni et al. [173].

$$\Delta V = \bar{A}_w * l + \left[\frac{1}{3} * \pi * \bar{D}^2(3R - \bar{D})\right] \quad (3.9)$$

In this equation, $\bar{D}$ stands for the mean depth of wear scar, $\bar{A}_w$ represents average area of cross-section of the wear scar, R denotes the radius of the zirconia ball, ΔV represents the overall volume loss, and l signifies the wear track length of the alloy. Additionally, the wear rate for each sample was calculated using Eq. (3.10).

$$W_v = \frac{\Delta V}{S} \quad (3.10)$$

Here, S denotes the overall sliding distance of the wear track and W_v indicate the wear rate in mm³/mm. After wear testing, SEM micrographs were used to study the worn surfaces of all samples in order to get insight into understanding of the wear process.

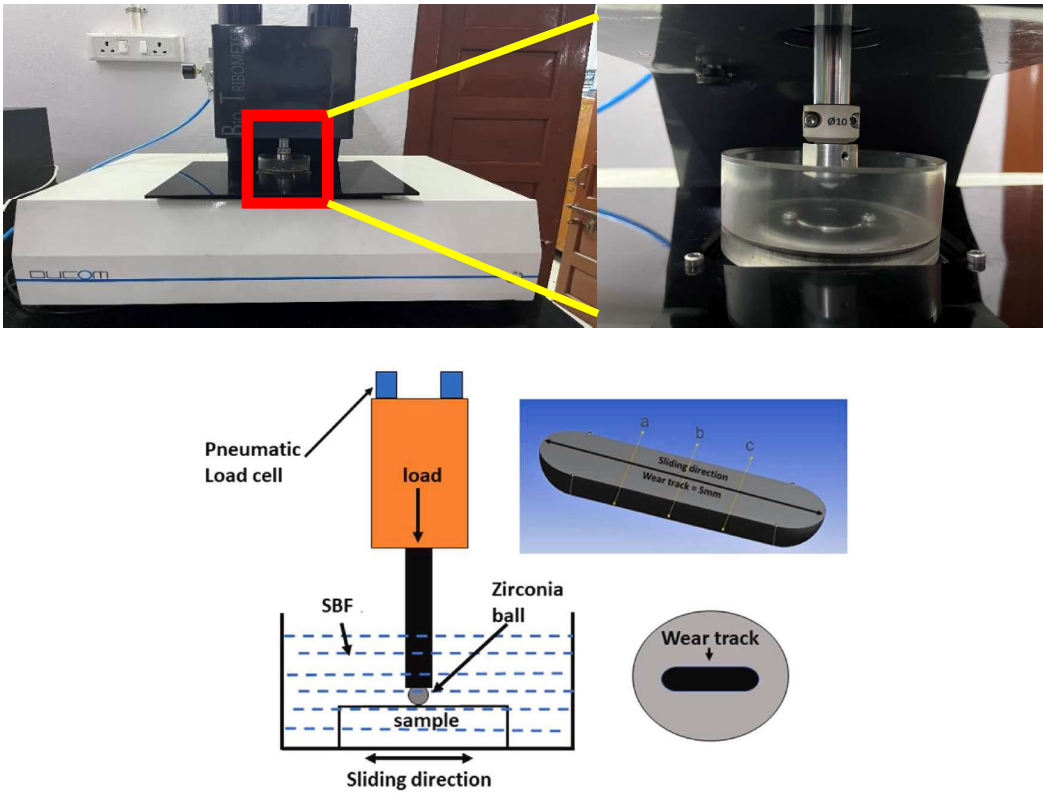

Fig. 3.10: Bio-Tribometer test setup and schematic track formation

3.8 Tribo-corrosion testing

Tribocorrosion testing of implant materials in SBF solution is a crucial method for evaluating the combined effects of mechanical wear and electrochemical corrosion on biomaterials. In this test, the implant material is subjected to both abrasive or sliding wear and an electrochemical environment that mimics the human body, typically by using a SBF with ionic concentrations similar to those of blood plasma. The test was performed on a mirror finished surface cleaned through acetone in ultrasonication. The alloy sample was immersed in SBF solution with pH of 7.4 and maintained at body temperature 37 ± 1 ℃. The test is conducted using a Bio-tribometer equipped with potentiostat with standard 3 electrode configuration (Biotribometer TR01, DUCOM Instruments Pvt. Ltd., India and Potentiostat, IVIUM Technologies, Netherland). The load is applied through upper spindle and lower bas, which holds the sample are allowed to reciprocate with specified parameters. The schematic diagram and image of the tribocorrosion test setup is shown in Fig. 3.11. Similar to corrosion testing, the sample acts as a working electrode, a graphite rod serves as a counter electrode, and Ag/AgCl as reference electrode. After all connections, OCP is conducted without any load for 3600 s. Then, two types of tribocorrosion test are conducted. The first type is OCP test, which conducted in three steps; step 1: OCP without any load for 600 s, step 2: OCP with applied load for 2400 s, and step 3: OCP with load removed for 600 s. The second type is potentiodynamic polarization test, which is conducted for the potential range from -1.5 V to 2.4 V with normal load of 20 N following the reciprocating motion profile with 5 mm track length at 1 Hz frequency.

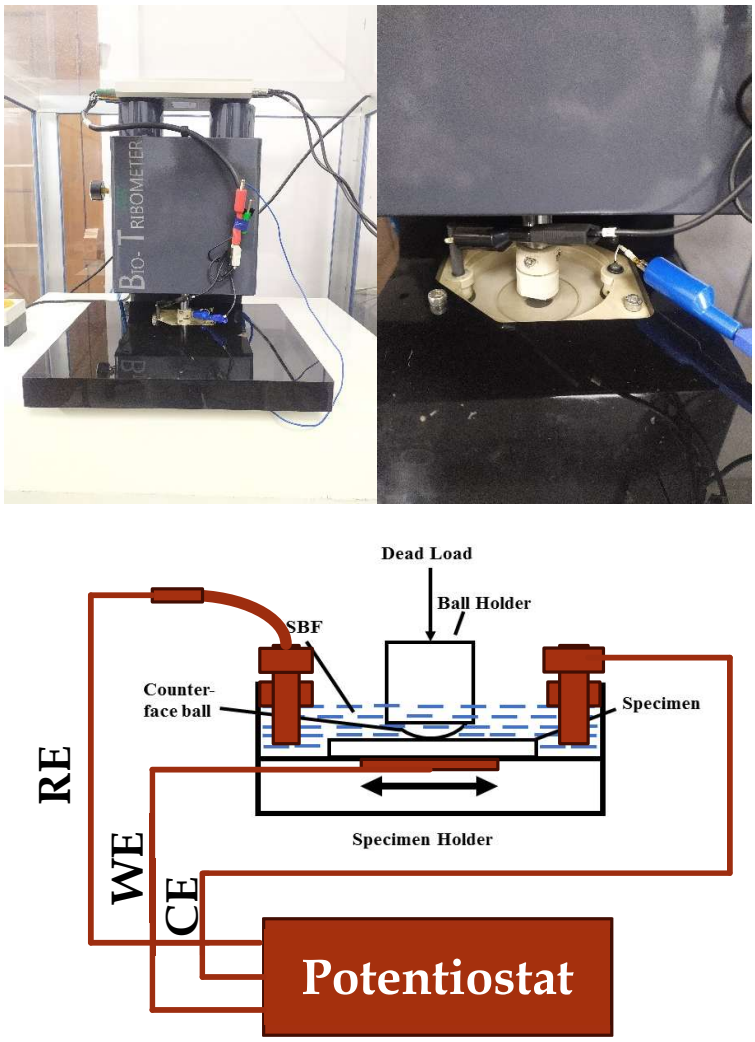

Fig. 3.11: Schematic diagram and image of the tribocorrosion test setup with a standard three-electrode system